A Planar Hybrid-geometry Wideband Antenna for Sub-6 GHz 5G Communications

Suthasinee Lamultree [1,*] and Chuwong Phongcharoenpanich [2]
[1] Department of Electronics and Telecommunication Engineering, Faculty of Engineering, Rajamangala University of Technology Isan Khonkaen Campus, Khonkaen, Thailand
[2] Department of Telecommunications Engineering, School of Engineering, King Mongkut's Institute of Technology, Ladkrabang, Bangkok, Thailand
Email: suthasinee.la@rmuti.ac.th (S.L.); chuwong.ph@kmitl.ac.th (C.P.)

Manuscript received April 8, 2026; revised May 6, 2026; accepted June 2, 2026; published September 222, 2026
*Corresponding author

***Abstract*—A planar wideband patch antenna based on a hybrid radiating structure is presented for sub-6 GHz Fifth-Generation (5G) and broadband wireless systems. The antenna combines a semi-circular radiator, a rectangular extension, dual L-shaped strips, and a modified partial ground plane to generate multiple closely spaced resonant modes. Interaction among these modes produces a continuous impedance response over a broad frequency range. The proposed antenna is implemented on a single-layer FR-4 substrate with overall dimensions of 46 mm × 58 mm × 1.6 mm. Measured results show a −10 dB impedance bandwidth from 1.77 GHz to 9.55 GHz, corresponding to a fractional bandwidth of 137.46%. Simulated and measured characteristics agree well across the operating region. Surface current analysis indicates that the broadband behavior originates from geometry-dependent current redistribution and coupling interaction between the radiator and the modified ground structure. The proposed antenna preserves consistent omnidirectional radiation behavior while providing simulated realized gains between 2.24 dBi and 5.28 dBi, together with radiation efficiency exceeding 72.8% throughout the operational spectrum. Owing to its simple planar configuration and wide operating range, the proposed design is suitable for sub-6 GHz wireless devices.**

***Index Terms*—hybrid-geometry, patch antenna, sub-6 GHz, wideband antenna, Fifth-Generation (5G) communications**

I. INTRODUCTION

As Fifth-Generation (5G) networks are rapidly implemented worldwide, there is a growing requirement for compact, high-performance antenna designs compatible with the sub-6 GHz band [1–6]. These frequency bands are pivotal for the ubiquitous connectivity required by the Internet of Things (IoT), autonomous vehicles, and satellite-integrated networks [7–11]. To meet the requirements of modern 5G terminals, antenna designs must simultaneously deliver wide impedance bandwidth, stable radiation patterns, and a low-profile footprint without escalating fabrication complexity [12–15].

Microstrip-based patch structures are frequently utilized in these scenarios, owing to their compact physical dimensions, straightforward production process, and seamless integration with planar circuitry [8, 16]. However, their inherently narrow bandwidth limits their applicability in broadband and multi-service communication systems. To broaden the bandwidth, researchers have implemented several design tactics. These encompass the use of slot-loading techniques and Defected Ground Structures (DGS), as well as the incorporation of parasitic elements. Additionally, fractal, metamaterial-inspired, and electromagnetic surface-assisted designs have shown significant promise [6–10, 14, 15, 17–24]. For instance, slot-based designs [6, 7] improve impedance matching by extending current paths, while combined radiator–ground modifications [8, 9] enhance bandwidth by perturbing current distribution and coupling mechanisms. Furthermore, fractal-based radiator geometries have been investigated to generate multiple resonant modes and support bandwidth enhancement through self-similar current distributions [14, 15]. Other bandwidth-improvement techniques, such as tapered feeding networks [17], array-based configurations [18, 22], and Metamaterial (MTM)-assisted implementations [24], have also been introduced to broaden the operating spectrum through impedance transformation and multi-mode excitation mechanisms. More recently, electromagnetic surface-engineering and MTM-inspired approaches have attracted increasing attention for improving impedance bandwidth and radiation performance. Representative examples include split-ring resonator (SRR)-loaded metamaterial structures [19], Artificial Magnetic Conductor (AMC)-integrated planar antennas [20], and Frequency Selective Surface (FSS)-assisted radiators employing parasitic elements [23]. Although these techniques are effective in improving bandwidth and gain performance, they frequently rely on additional electromagnetic layers, parasitic structures, or increased electrical size, which can complicate fabrication and influence radiation characteristics [25, 26].

Equivalent-circuit interpretations have also been employed to explain the interaction among resonant modes in compact wideband antennas [22–24]. These studies indicate that distributed inductive-capacitive coupling between the radiator and ground structure plays an important role in generating broadband impedance characteristics. Nevertheless, achieving wideband operation using a compact single-layer planar structure with stable radiation behavior remains a continuing challenge for sub-6 GHz 5G systems.

Hybrid-geometry antennas have emerged as a robust alternative, leveraging multiple shapes to excite broader resonances [27, 28]. Even with the recent evolution of 5G antenna technologies, a prominent research gap continues to challenge the field, as most existing hybrid designs prioritize bandwidth at the expense of structural simplicity or lack a clear physical interpretation of the operating mechanism [29, 30]. Furthermore, recent literature often emphasizes numerical results while providing limited insight into the mode-coupling dynamics responsible for impedance matching [31–33].

However, unlike existing hybrid-geometry designs that primarily rely on geometric combination to enhance bandwidth, the proposed structure explicitly links geometry-induced current redistribution to the formation of a continuous impedance band. This provides clearer physical interpretability of the operating mechanism and supports a more systematic design approach. In response to this need, a Planar Hybrid-Geometry Wideband Antenna (PHGWA) is developed for sub-6 GHz 5G applications, offering a balance between size and performance. By combining various geometric elements on the main radiator and utilizing an altered partial ground structure, the design facilitates adjacent resonant-mode coupling, thereby achieving a wide impedance bandwidth without requiring multilayer fabrication, stacked radiators, defected superstrates, or additional parasitic arrays. In this work, structural complexity refers to the necessity for multilayer structures, external parasitic elements, stacked radiators, or additional electromagnetic loading layers that increase fabrication difficulty and integration cost.

Specifically, this study contributes to the field in the following ways:

- A planar hybrid-geometry antenna suitable for sub-6 GHz 5G applications and extended wideband applications is proposed, enabling broadband performance within a simple planar structure.
- A wide −10 dB fractional bandwidth of 137% is achieved using a cost-effective single-layer FR-4 substrate, avoiding the need for multilayer configurations or parasitic components.
- The design evolution and surface current analyses provide insight into the electromagnetic mechanism underlying bandwidth enhancement, indicating that the observed wideband behavior is associated with mode coupling enabled by the hybrid geometry and modified ground plane.
- Experimental measurements confirm stable omnidirectional radiation patterns with moderate gains, demonstrating that this antenna is well-suited for the requirements of sub-6 GHz 5G communication systems.

II. Design Evolution / Working Mechanism

A. Design Layout

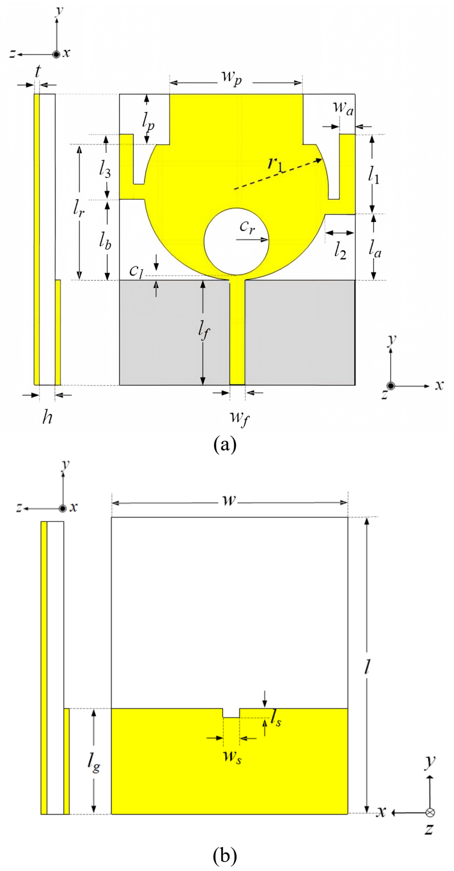

Fig. 1. Structural configuration of the PHGWA: (a) front perspective, (b) back perspective.

The structural configuration of the proposed PHGWA is presented in Fig. 1, with sub-figures (a) and (b) depicting the front and back perspectives, respectively. The radiating structure consists of a hybrid geometry formed by a semi-circular patch with radius r_1 integrated with a rectangular section of width w_p and length l_p. To refine the flow of current and optimize impedance matching, a round notch with a radius denoted by c_r is carved into the central region of the hybrid radiator, positioned at a distance c_l from the bottom boundary. In addition, two asymmetric L-Shaped Strips (LSSs) are incorporated near the lower edge of the radiating element to enhance bandwidth performance. Each strip has a thickness w_a and horizontal length l_2, while the vertical arms have unequal lengths l_1 and l_3, positioned at l_a and l_b on the right and left sides of the patch, respectively. All radiating elements are implemented using a copper layer with thickness t. To achieve signal excitation, the design utilizes a microstrip transmission line with a characteristic impedance of 50 Ω, having a width of w_f and a length of l_f. The entire structure is fabricated on an FR-4 substrate with a relative permittivity of 4.3 and thickness h=1.6 mm, while the overall substrate size is 46 mm × 58 mm ×0.16 mm. The bottom layer employs a partial ground plane with a width w_g=w and length l_g, incorporating a centrally positioned narrow-rectangular slot (width w_s, length l_s), which is pivotal in tailoring the impedance bandwidth through the alteration of the return current trajectories and the strengthening of the electromagnetic interaction between the patch and the ground.

The antenna geometry, including the Subminiature Version A (SMA) connector effects, was modeled and numerically optimized using the Computer Simulation Technology (CST) Studio Suite. To ensure simulation accuracy, open (add space) boundary conditions were applied in all directions to emulate a free-space environment. Design parameters were iteratively adjusted to achieve a reflection coefficient $|S_{11}| < -10$ dB across the target band (2 GHz to 6 GHz) while preserving consistent radiation properties and a realized gain exceeding 2.5 dBi. This comprehensive simulation approach accounts for the practical transition between the feed line and the measuring equipment, contributing to the high correlation between the simulated results and the performance observed in the final prototype. The final design parameters for the proposed antenna architecture are detailed in Table I. In this work, the term "hybrid-geometry" denotes the integration of a semi-circular radiator, asymmetric L-Shaped Strip Arms (LSSAs), a circular groove, and a modified ground structure within a unified planar radiating configuration.

TABLE I: OPTIMIZED PARAMETER VALUES FOR THE PHGWA

Symbol	Dimension (mm)	Symbol	Dimension (mm)	Symbol	Dimension (mm)
w	46	l_r	27	l_1	16
l	58	c_r	7	l_2	7
r_1	18	c_l	1	l_3	13
w_f	3	l_s	2	w_a	3
l_f	21	w_s	3	w_p	21
l_g	21	l_a	13	l_p	10
w_g	46	l_b	16		

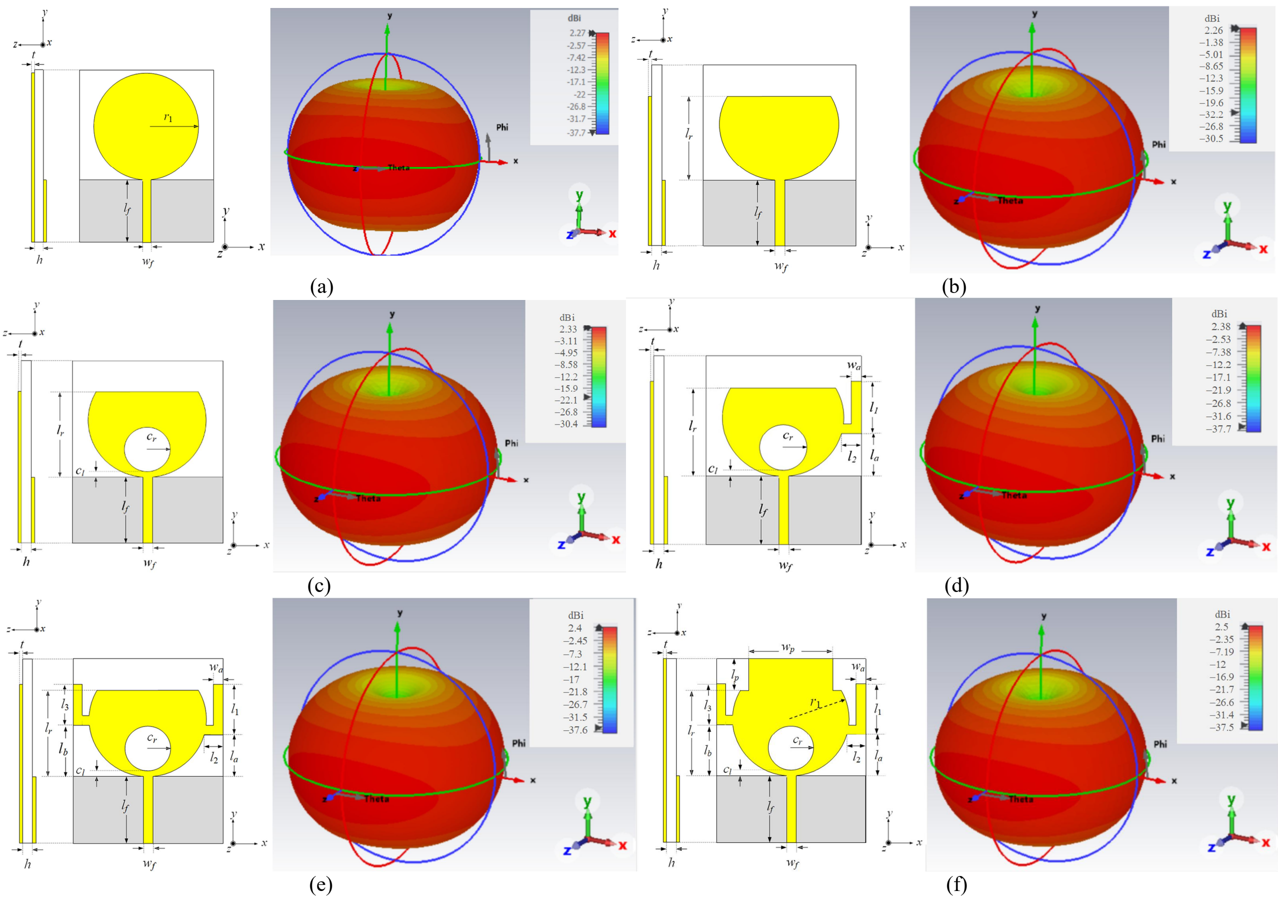

Fig. 2. The developed antenna and its radiation: (a) Ant#1, (b) Ant#2, (c) Ant#3, (d) Ant#4, (e) Ant#5, and (f) proposed PHGWA.

B. Antenna Evolution and Design Rationale

The wideband PHGWA was systematically developed through a six-stage evolutionary design process, as depicted in Fig. 2, with each stage aimed at improving impedance bandwidth, radiation characteristics, and antenna gain. In the initial stage, Antenna #1 (as shown in Fig. 2(a)) was configured with a standard circular radiator with a radius (r_1) of 18 mm, as determined by the guidelines in [34]. The design was realized on an FR4 substrate (1.6 mm thickness) with an overall footprint of 46 mm × 58 mm. A 50-Ω microstrip feed line, optimized for 2 GHz resonance, features a w_f of 3 mm and a l_f of 21 mm [35]. To facilitate broadband performance, a partial ground plane (l_g = 21 mm) was employed to induce capacitive coupling between the radiator and the ground structure [34], yielding an initial realized gain of 2.27 dBi and an omnidirectional radiation pattern.

To enhance the impedance bandwidth, Antenna #2 was derived by truncating the upper portion of the circular patch, thereby forming a semicircular radiator, observing in Fig. 2(b). This modification altered the effective current flow paths and reduced the quality factor (*Q*) of the resonant structure, thereby enhancing impedance matching across a wider frequency range. A marginal reduction in gain to 2.26 dBi was observed, attributed to the slightly decreased effective radiating aperture.

In the third stage (Antenna#3 in Fig. 2(c)), a 7-mm-radius circular groove was integrated into the semi-circular radiating element, maintaining a vertical offset of 1 mm from the patch's base. This modification introduces reactive loading, which perturbs the current path length and introduces additional resonance, contributing to bandwidth extension. Simultaneously, a narrow rectangular slot is centered along the top of the partial ground plane. The dimensions of this opening are defined by a width (w_s) of 3 mm and a length (l_s) of 2 mm. This slot enhances electromagnetic coupling between the radiating patch and the ground plane by locally modifying the current return path, thereby improving impedance matching, particularly in the transition region between adjacent resonant modes.

Further enhancement in gain and lowering the operating frequency was achieved in Antenna #4 (Fig. 2(d)) by attaching a right-side LSSA to the radiating patch. This structure effectively increased the electrical length and promoted stronger surface current concentration, resulting in a gain improvement to 2.32 dBi. However, the asymmetric current distribution caused a slight tilt in the omnidirectional radiation pattern.

To restore radiation symmetry, a second LSSA with identical width and horizontal length but adjusted vertical length and position was implemented on the opposing side of the radiator to rectify radiation asymmetry, as illustrated in Fig. 2(e). This configuration balanced the surface current distribution, yielding a symmetric omnidirectional radiation pattern while maintaining the enhanced gain of 2.4 dBi, confirming the importance of structural symmetry in stable radiation performance.

In the final stage (Fig. 2(f)), a rectangular strip was integrated along the radiator's top edge to extend the current path and enhance radiation at lower operating frequencies. The completed PHGWA configuration achieved an optimized gain of 2.5 dBi at 2 GHz, delivering a robust balance between a wideband response and stable radiation characteristics.

Fig. 3 summarizes the impedance matching characteristics (at the −10 dB threshold) throughout the antenna's design stages, suggesting that the observed wideband performance is associated with systematic modification of surface current paths rather than purely empirical tuning. The baseline Antenna #1 exhibits two separated impedance bands (1.81 GHz to 2.46 GHz and 3.54 GHz to 6.13 GHz) due to the limited current paths of the conventional circular patch. Truncating the patch in Antenna #2 redistributes surface currents along the modified edge, improving impedance matching and extending bandwidth without altering the omnidirectional radiation behavior. A substantial bandwidth enhancement is achieved in Antenna #3 by introducing a circular groove on the radiator and a slot on the partial ground plane, which strengthens radiator–ground structure coupling and excites multiple resonant modes, yielding a continuous wideband response from 1.94 GHz to 6.73 GHz. The integration of the LSSA in Antennas #4 and #5 further elongates the effective electrical length, significantly shifting the lower resonance edge and improving impedance matching across the higher spectrum, from 1.86 GHz to 7.84 GHz and 1.81 GHz to 8.93 GHz for Antennas #4 and #5, respectively. By hybridizing these optimized features, the final PHGWA achieves a continuous wideband impedance bandwidth from 1.67 GHz to 8.95 GHz while maintaining stable omnidirectional radiation and competitive gain of 2.5, 3.52, and 3.41 dBi at 2, 4, and 6 GHz, respectively, confirming that the deep $|S_{11}|$ minima directly correspond to efficient radiation rather than reactive energy storage. The detailed numerical results of each stage are summarized in Table II.

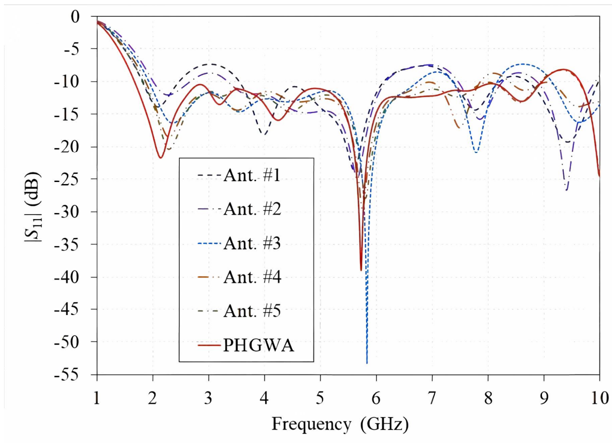

Fig. 3. Comparing the simulated $|S_{11}|$ of the developed antenna.

TABLE II: COMPARED ANTENNA PERFORMANCE OF THE DEVELOPED ANTENNA

Antenna	Simulated −10 dB Bandwidth	Gain (dBi)		
		f = 2 GHz	*f* = 4 GHz	*f* = 6 GHz
#1	1.81–2.46 GHz, 3.54–6.13 GHz	2.27	3.58	3.90
#2	2–2.66 GHz, 3.33-6.16 GHz	2.26	2.54	3.34
#3	1.94–6.73 GHz	2.33	2.98	2.85
#4	1.86–7.84 GHz	2.38	3.02	3.39
#5	1.81-8.93 GHz	2.4	2.82	3.64
PHGWA	1.67-8.95 GHz	2.50	3.52	3.41

C. Equivalent Circuit

A lumped-element equivalent circuit model elucidates the broadband characteristics of the proposed PHGWA, as shown in Fig. 4. The equivalent circuit provides a simplified interpretation of the electromagnetic behavior by representing the radiating and perturbation sections using lumped reactive and resistive elements. The excitation source is represented by a 50-Ω input port together with a series RL branch modeling the SMA connector and feed transition. The microstrip feed line employs cascaded RL sections with shunt capacitive elements to mimic distributed transmission-line behavior. The rectangular defect in the ground plane is modeled as a parallel LC resonator, enhancing impedance matching at lower frequencies. Similarly, the circular groove is represented by an additional parallel LC branch, affecting surface current distribution and supporting higher-order resonant excitation for broadband operation.

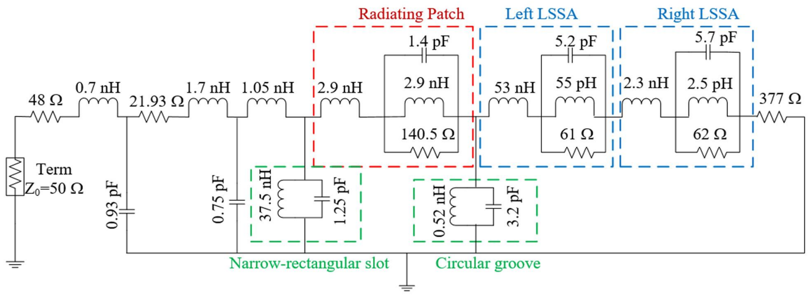

Fig. 4. Lumped-element equivalent circuit model of the proposed PHGWA.

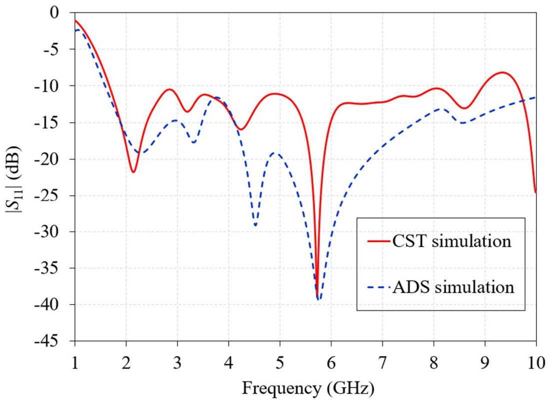

Fig. 5. Compared simulated $|S_{11}|$ from CST and Advanced Design System (ADS).

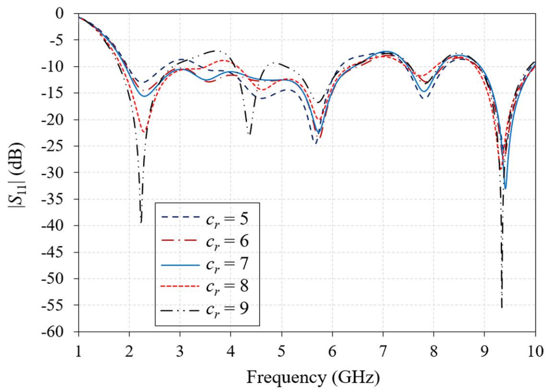

Fig. 6. Effect of c_r on $|S_{11}|$.

The main radiating patch is defined by a resonant circuit with Resistor(R), Inductor(L), and Capacitor(C). This network integrates a series of inductive elements with parallel RLC components, which govern the antenna's dominant resonance and energy storage. The radiation resistance reflects the power emitted into free space. The left and right LSSAs are characterized by supplementary parallel RLC resonators that extend current paths and induce inter-element coupling, generating multiple adjacent resonant modes. Mutual coupling among the resonant branches produces a broadened impedance profile and preserves acceptable radiation behavior throughout the Sub-6 GHz region. Ultimately, the total radiation resistance represents the equivalent free-space radiation loss of the antenna system. The integrated response of these resonant elements generates multiple adjacent resonances, enabling continuous impedance matching over the targeted Sub-6 GHz spectrum.

The proposed equivalent-circuit model substantiates that the broadband response arises mainly from the coupling interaction between the hybrid radiating structure and the modified ground plane. Similar multi-resonant circuit behaviors have been documented in [22–24]. The initial lumped-element values were derived from the formulation in [23], followed by parameter optimization using Advanced Design System (ADS). The optimized equivalent-circuit response closely aligns with the CST full-wave simulated $|S_{11}|$ characteristic, as depicted in Fig. 5.

D. *Parametric Study*

To further clarify the operating mechanism of the proposed PHGWA, a parametric investigation was conducted by varying several critical geometrical parameters associated with the hybrid radiator and modified ground structure. The effects of the circular groove radius (c_r), ground-slot length (l_s), and the dimensions and positions of the LSSAs were examined in terms of the reflection coefficient characteristics, as presented in Figs. 6–10.

Fig. 6 illustrates the influence of the circular groove radius c_r on the impedance response. The groove introduces reactive loading perturbation into the radiator and modifies the effective surface-current distribution, thereby affecting the higher-order resonant modes. As c_r varies from 5 mm to 9 mm, noticeable shifts in the resonant behavior are observed, particularly within the sub-6 GHz region. Among the investigated cases, $c_r = 6$ mm and $c_r = 7$ mm satisfy the $|S_{11}| < -10$ dB criterion over the desired operating band. However, $c_r = 7$ mm provides more stable impedance matching and more continuous resonance coupling across the wideband region. Therefore, $c_r = 7$ mm was selected for the optimized design.

The effect of the narrow rectangular slot length l_s embedded in the partial ground plane is presented in

Fig. 7. The slot alters the return-current trajectory and enhances the electromagnetic coupling between the radiator and the ground structure. For comparison, l_s = 0 mm represents the configuration without the ground slot. Increasing l_s significantly improves the impedance response at the upper operating frequencies due to enhanced radiator–ground structure interaction. Although several values exhibit similar wideband behavior, l_s = 2 mm produces the deepest resonance around 5.8 GHz while maintaining continuous impedance matching across the operating band. Consequently, l_s = 2 mm was adopted in the final configuration.

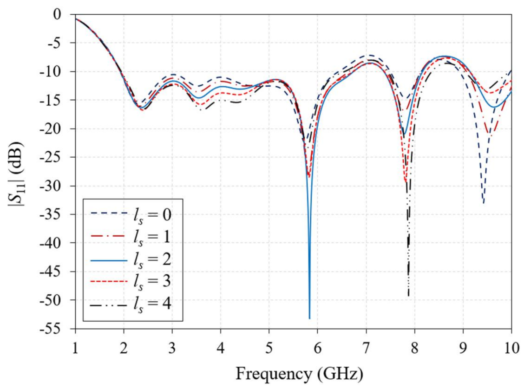

Fig. 7. Effect of l_s on $|S_{11}|$.

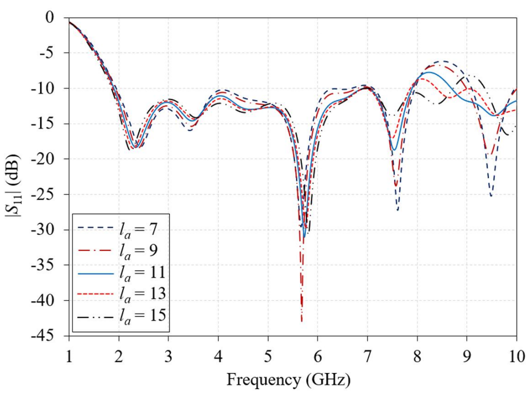

Fig. 8. Effect of l_a on $|S_{11}|$.

To improve the lower-frequency impedance response, a right-side LSSA was incorporated into the hybrid radiator. The total strip length approximately corresponds to a quarter-wavelength at 2 GHz [36], thereby extending the effective current path. Fig. 8 presents the influence of the strip position l_a on the reflection coefficient. Increasing l_a shifts the lower resonant edge toward lower frequencies due to the increased electrical path length, resulting in broader impedance coverage. In contrast, smaller values of l_a move the resonance upward and reduce the effective bandwidth. Although l_a = 9 mm generates a deeper resonance near 5.8 GHz, impedance matching around the mid-band region becomes less stable. By comparison, l_a = 13 mm provides more balanced wideband performance and was therefore selected. It was also observed that the single right-side strip introduces a slight radiation asymmetry due to the uneven current distribution.

To improve radiation balance and maintain stable omnidirectional characteristics, an additional LSSA was introduced on the left side of the radiator. Fig. 9 demonstrates the effect of varying l_3 from 10 mm to 22 mm. This parameter primarily controls the effective electrical length associated with the lower resonant mode. Increasing l_3 shifts the resonance toward lower frequencies; however, excessively large values produce undesired resonance displacement and impedance discontinuity. Among the investigated cases, l_3 = 13 mm achieves the most balanced response, providing stable wideband matching without excessive resonance distortion.

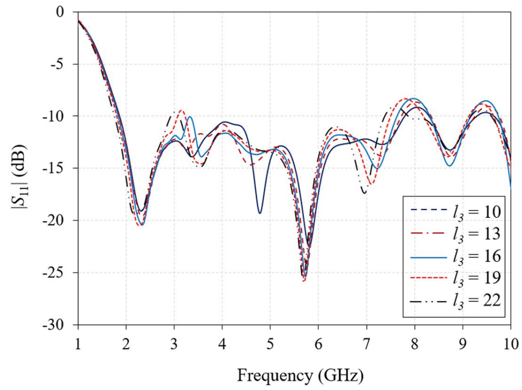

Fig. 9. Effect of l_3 on $|S_{11}|$.

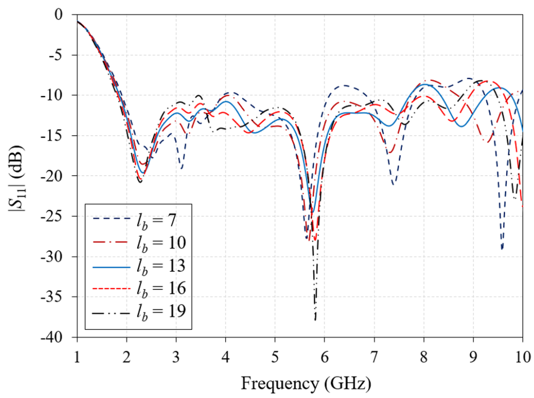

Fig. 10. Effect of l_b on $|S_{11}|$.

With l_3 fixed at 13 mm, the position parameter l_b was further optimized, as illustrated in Fig. 10. Adjusting l_b influences the coupling interaction between the left strip and the main radiator. The optimized value of l_b = 16 mm produces improved impedance continuity across the mid-band region and generates deeper resonant minima compared with the other investigated cases. The combined optimization of the LSSA dimensions and positions contributes significantly to the broadband response of the proposed antenna.

It should be noted that the rectangular extension added along the upper edge of the radiator mainly contributes to current-path elongation and radiation enhancement, particularly at lower frequencies. For reproducibility, all optimized design parameters are summarized in Table I, while the complete antenna evolution process is described in Section II-B.

The obtained parametric results demonstrate that the antenna operation is dominated by interacting resonant modes and spatial current redistribution instead of a single isolated resonance.

E. Surface Current Distribution and Performance Correlation

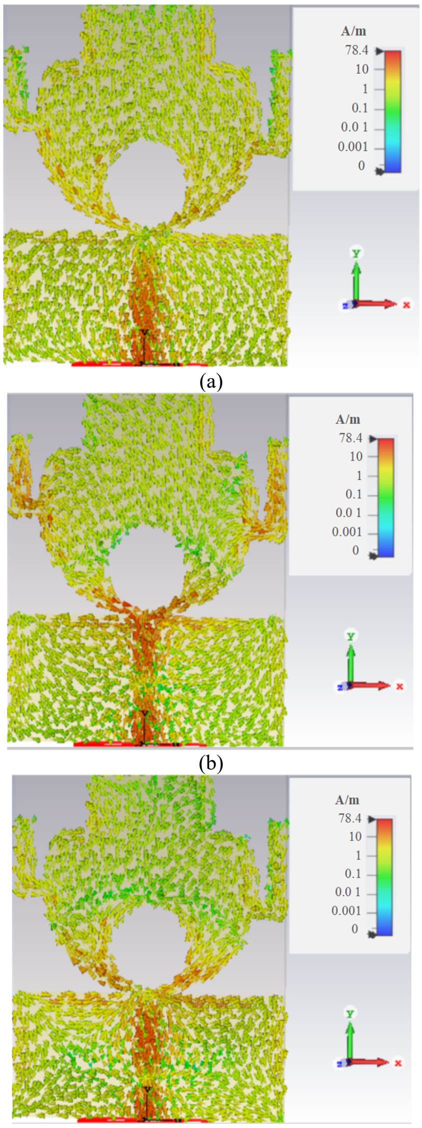

Fig. 11. Current distribution patterns of PHGWA at: (a) 2 GHz, (b) 4 GHz, (c) 6 GHz.

To further elucidate the physical mechanism behind the proposed PHGWA response, the simulated surface current behavior across the developed antenna structure is analyzed at 2 GHz, 4 GHz, and 6 GHz, as illustrated in Fig. 11. These frequencies represent the fundamental and higher-order resonant modes across the operational spectrum. At 2 GHz, surface currents are strongly concentrated along the microstrip feed and the gap between the feeder and the ground plane structure junction, with pronounced current distribution over the radiating patch, confirming excitation of the fundamental resonant mode. This current distribution corresponds well to the lower-band $|S_{11}|$ resonance, indicating efficient impedance matching. The resulting dominant vertical current path supports stable broadside radiation with moderate realized gain.

With the frequency rising toward 4 GHz, the current distribution becomes more distributed from the feedline across the hybrid radiator, with significant intensification detected around the periphery of the round groove and the LSSAs. This indicates the activation of a coupled higher-order mode that overlaps with the fundamental mode and contributes to impedance-bandwidth broadening, as observed in the wide $|S_{11}|$ <-10 dB region. This distributed current behavior also contributes to improved radiation strength within the mid-band region.

At 6 GHz, intense surface currents are localized along the upper patch edges, slots, and truncated ground-structure boundaries, revealing the excitation of another higher-order resonant mode. This current concentration explains the maintained impedance matching at the upper band. In contrast, the edge-concentrated currents contribute to stable radiation behavior with increased gain due to higher effective aperture utilization.

Overall, the analyzed current distributions indicate that the broadband characteristic is achieved through resonant-mode interaction between the hybrid radiator and the defected ground configuration. The distributed current paths across different frequency regions contribute to stable impedance characteristics and consistent radiation behavior throughout the operating band.

F. Discussion and Analysis $|S_{11}|$ and Gain Performance

Fig. 12 illustrates that the extended operating bandwidth of the PHGWA originates from the excitation of multiple closely spaced resonant modes instead of conventional single-resonance operation. The antenna maintains simulated $|S_{11}| < -10$ dB from 1.67 GHz to 8.95 GHz, covering the entire sub-6 GHz band and extending into higher frequencies. Multiple resonances are observed across the band, with a pronounced impedance minimum of approximately −39 dB near 5.7 GHz, indicating that multiple closely spaced resonant modes are effectively merged to form a continuous impedance bandwidth. The presence of several resonance minima, including a pronounced dip around 5.7 GHz, suggests strong electromagnetic interaction between the hybrid radiating structure and the modified ground plane. These resonances are not independent; instead, their interaction leads to distributed impedance matching across the operating band. The moderate ripple observed in the $|S_{11}|$ response reflects partial modal overlap, which is characteristic of wideband antennas based on multi-mode coupling.

The realized gain exhibits frequency-dependent behavior consistent with the radiator's electrical size. At lower frequencies, the electrically small aperture limits radiation, resulting in modest gain (~2 dBi). As frequency increases, improved current confinement along the patch edges, grooves, and ground-structure discontinuities enhances radiation efficiency, leading to a maximum gain of nearly 5.28 dBi at about 4.8 GHz. At higher frequencies, slight gain fluctuations are observed, which can be attributed to the excitation of higher-order modes and partial pattern distortion.

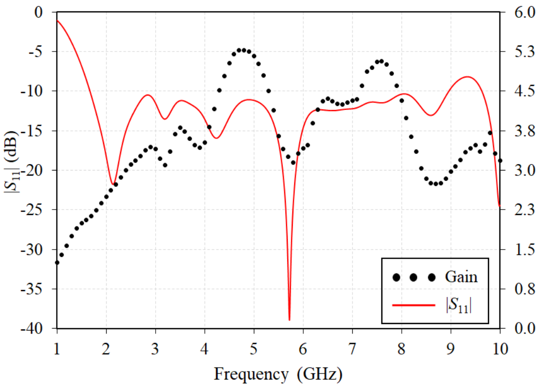

Fig. 12. Simulated $|S_{11}|$ and gain versus frequency for the proposed PHGWA.

Although minima in $|S_{11}|$ generally coincide with improved gain, the correlation is not strictly monotonic across the band, indicating that different modal contributions influence impedance matching and radiation efficiency. Nevertheless, the gain variation remains within an acceptable range across the sub-6 GHz band, confirming that the proposed design achieves broadband operation without significant degradation in radiation performance. This indicates that the bandwidth enhancement is governed by distributed modal interactions, while radiation efficiency is additionally constrained by frequency-dependent current confinement and pattern stability.

III. Experimental Results and Their Implications

To experimentally demonstrate, the proposed PHGWA architecture was manufactured as a prototype on a cost-effective FR4 substrate (ε_r = 4.3) with dimensions specified in Table I. The fabricated antenna, depicted in Fig. 13(a) and Fig. 13(b), was fed via a 50-Ω SMA connector for coaxial excitation. The reflection coefficient ($|S_{11}|$), radiation patterns, and gain were measured using an E5063A network analyzer, as depicted in Fig. 13(c). To ensure high fidelity and minimize external interference, radiation characteristics were characterized within a controlled electromagnetic environment. The measurement framework employed a pair of identical PHGWAs acting as the transmitter antenna and the receiving antenna (Antenna Under Test (AUT)). The AUT was integrated onto a high-precision turntable featuring a 1°-step size. Furthermore, a bore-sight separation of 30 cm was established to strictly adhere to the Fraunhofer distance requirements (a calculated distance of 21.92 cm at 6 GHz).

Comparison between the simulated and measured $|S_{11}|$ results is presented in Fig. 14(a), while the gain and radiation efficiency characteristics are illustrated in Fig. 14(b). Good agreement is observed, indicating that the proposed design captures the essential electromagnetic behavior. Minor discrepancies can be attributed to practical factors such as SMA soldering effects, fabrication tolerances, and variations in the FR-4 substrate material. The measured −10 dB impedance bandwidth spans 1.77 GHz to 9.55 GHz (137.46%), which is consistent with the simulated response (1.67 GHz to 8.96 GHz (137.16%)) and confirms the wideband operation of the antenna.

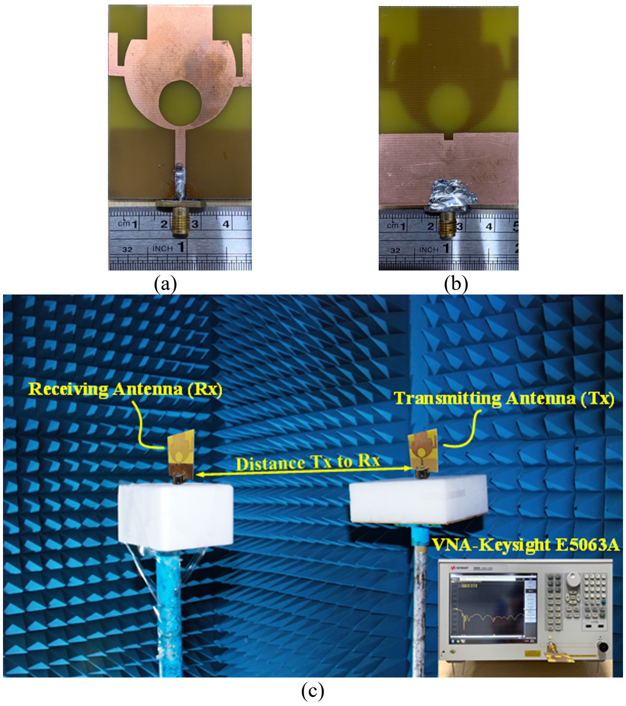

Fig. 13. Physical model: (a) upper layer configuration, (b) ground-plane side, (c) $|S_{11}|$ and radiation pattern setup.

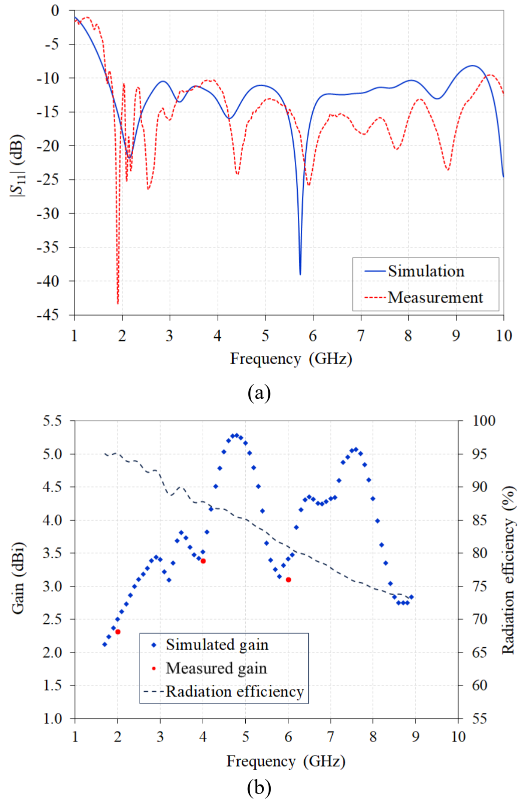

Fig. 14. Validation of PHGWA performance: (a) simulated and measured $|S_{11}|$ and (b) gain and radiation efficiency.

Regarding radiation characteristics, the proposed PHGWA exhibits stable gain and high radiation efficiency throughout the operating band. Simulated peak gains of 2.50 dBi at 2 GHz, 3.52 dBi at 4 GHz, and 3.41 dBi at 6 GHz were obtained, with corresponding radiation efficiencies of 95.01%, 87.76%, and 80.96%, respectively. The measured gains of 2.32 dBi, 3.39 dBi, and 3.10 dBi at the same frequencies show good agreement with the simulated results. The slight gain reduction in measurements is primarily due to dielectric losses and connector-related parasitics. Over the investigated frequency range, the antenna provides simulated realized gains between 2.24 dBi and 5.28 dBi, together with acceptable radiation efficiency and consistent radiation behavior.

The measured and simulated results consistently demonstrate that the proposed PHGWA achieves broadband operation through controlled multi-mode coupling while maintaining satisfactory radiation efficiency. The close agreement between simulation and measurement also validates the practical realizability of the proposed configuration for Sub-6 GHz wideband wireless applications.

The radiation characteristics of the proposed PHGWA were experimentally evaluated at 2, 4, and 6 GHz within the *xz* and *yz* orientations using identical antennas for transmission and reception. The measured results exhibit strong agreement with simulations, validating the accuracy of electromagnetic modeling and modal prediction. At 2 GHz, the antenna demonstrates a stable omnidirectional radiation profile in the *xz*-plane and a classic figure-of-eight distribution within the *yz*-orientation, as evidenced by Fig. 15(a) and Fig. 15(b), respectively. The 3D radiation plot further verifies broadside-dominant radiation with uniform azimuthal coverage. This behavior corresponds to the fundamental resonant mode, where surface currents are primarily distributed along the main radiating edges, producing symmetric radiation.

At 4 GHz, a nearly omnidirectional response is maintained, as plotted in Fig. 16(a), with slight asymmetry displayed in the principal *xz*-plane, as evidenced by Fig. 16(b). This minor distortion can be attributed to the onset of hybrid mode interaction between the patch and the modified ground structure. The preservation of the figure-eight pattern in the *yz*-plane (Fig. 16(c)) indicates that radiation symmetry is largely maintained despite modal coupling.

At 6 GHz, slight pattern splitting is observed in the 3D radiation profile as shown in Fig. 17(a), indicating increased contribution from higher-order or hybridized modes. However, the 2D cuts in both principal planes (Fig. 17(a) and Fig. 17(b)) retain a broad omnidirectional behavior, demonstrating that multi-mode excitation enhances bandwidth without significantly degrading radiation stability.

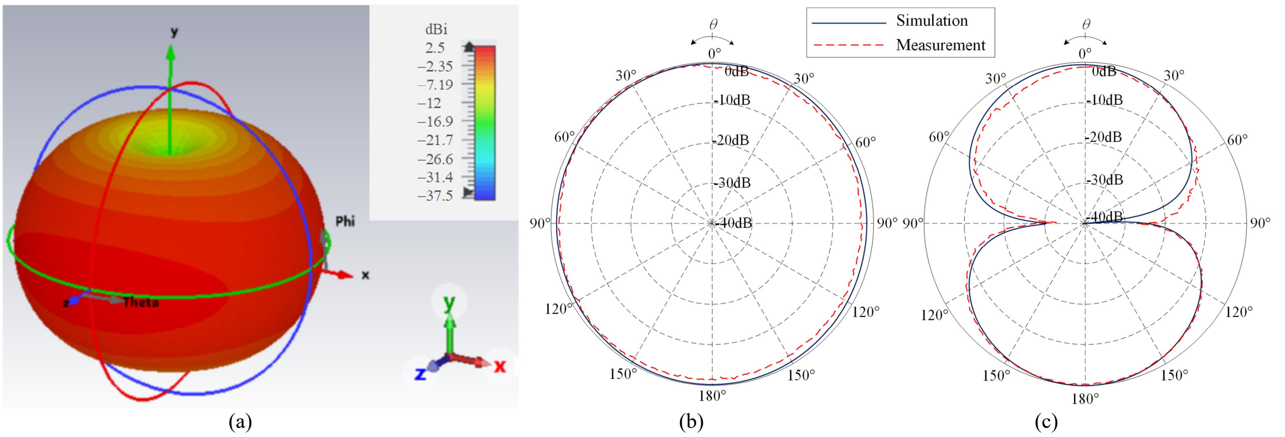

Fig. 15. Simulated and measured radiation patterns at 2 GHz: (a) 3D, (b) *xz*-plane, and (c) *yz*-plane.

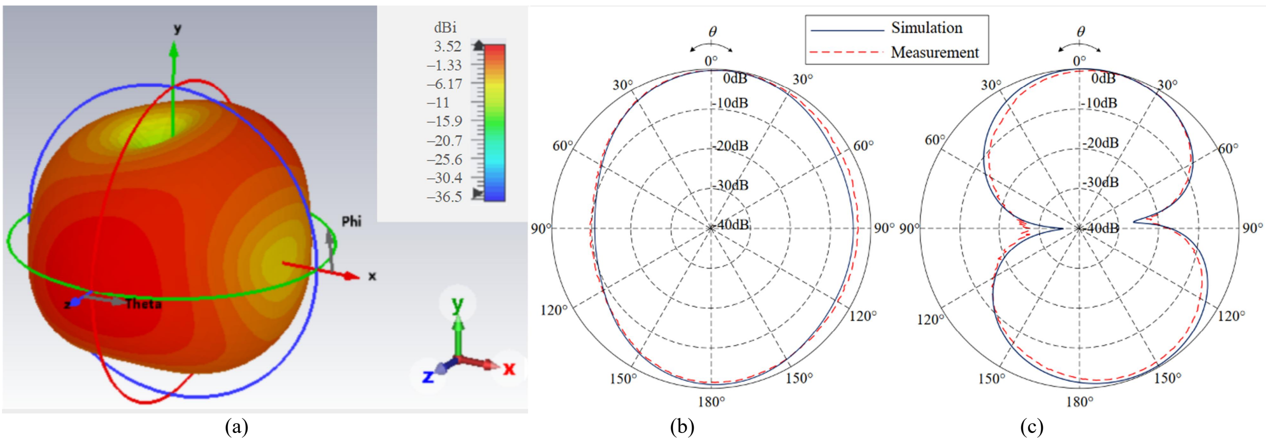

Fig. 16. A comparison between the simulated and experimental radiation characteristics at 4 GHz: (a) 3D, (b) *xz*-plane, and (c) *yz*-plane.

The antenna maintains stable linear polarization characteristics across the operating band, with cross-polarization levels below –22 dB and a comparatively large axial ratio response. Over the sub-6 GHz frequency region, the realized gain varies between 2.24 dBi and 5.28 dBi, while the simulated radiation efficiency remains within the range of 72.8%–95%. These results indicate that the proposed hybrid-geometry antenna achieves broadband performance through distributed multi-mode excitation and modal interaction while preserving stable radiation behavior throughout the operating spectrum.

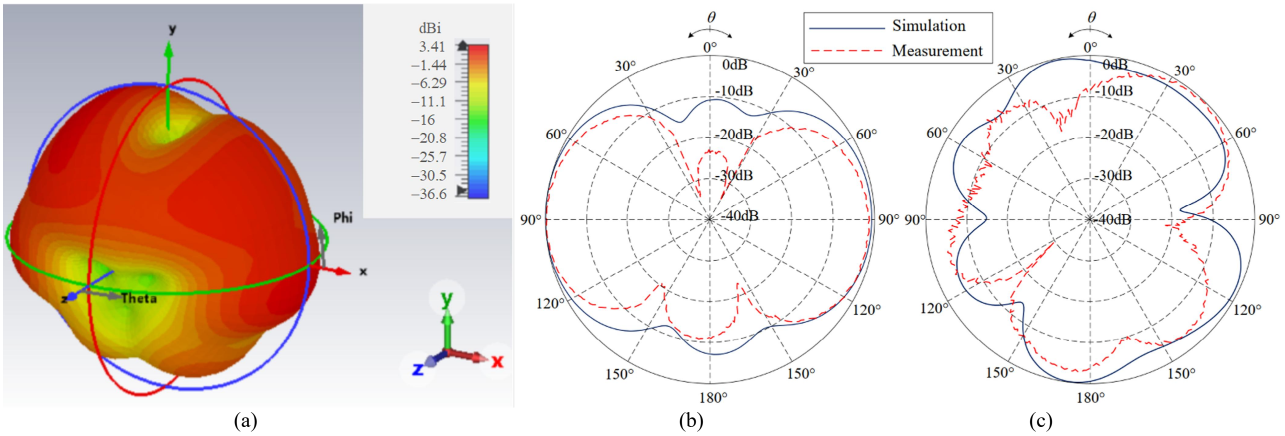

Fig. 17. A comparison between the simulated and experimental radiation characteristics at 6 GHz: 3D, (b) *xz*-plane, and (c) *yz*-plane.

The proposed antenna performance is benchmarked with recently reported Sub-6 GHz wideband antennas, as summarized in Table III, considering key metrics such as physical footprint, operating bandwidth, and design intricacy. To facilitate a fair benchmark, all physical parameters of the antenna are expressed in terms of the free-space wavelength (λ_L) corresponding to the lower-bound frequency. The comparison indicates that the proposed PHGWA provides a wide operating bandwidth while maintaining a planar single-layer configuration and omnidirectional radiation behavior. In contrast to the slotted patch configuration in [6], the proposed structure achieves broader spectral coverage without relying on multiple resonant slot sections. The semi-arc radiator reported in [9] demonstrates compact implementation and acceptable efficiency; however, its operational bandwidth remains comparatively narrower. Although the transparent MIMO antenna in [13] offers mechanical flexibility and optical transparency, its realized gain and minimum radiation efficiency are lower than those of the proposed design. The fractal antenna in [14] exhibits ultra-wideband characteristics, but detailed validation of radiation stability and measured efficiency across the operating band is limited.

TABLE III: COMPARATIVE PERFORMANCE EVALUATION WITH RECENT SUB-6 GHZ WIDEBAND ANTENNAS

Ref.	Antenna type and applied technique	Material	Dimension (λ_L/ mm)	Bandwidth (−10 dB)	Pattern	Structure complexity	Gain (dBi)	Eff (%)
[6]	Slotted patch and partial ground plane	R04003C	0.21× 0.14× 0.007/ (26 × 17 × 0.813 mm^3)	2.44–5.74 GHz	omnidirectional	Medium (planar)	2	n/a
[9]	Semi arc-shaped stub integrated modified circular radiator + CPW	PET	0.61×0.46×0.002/ (40 × 30 × 0.1 mm^3)	4.57–5.50 GHz,	omnidirectional	Low (planar)	3.8	81–90
[13]	Transparent antenna with circular stub-loaded C-shaped + partial ground plane (4 elements MIMO)	AgHT-4 &Melinex (ST507)	0.33×0.48×0.005/ (45×66×0.635 mm^3)	2.21–6 GHz	omnidirectional	Medium (bending)	0.53	41 (min)
[14]	Fractal antenna	FR4	0.21×0.28×0.01/ (35×47×1.6 mm^3)	1.8–30 GHz	omnidirectional	Medium (planar)	5	n/a
[19]	Metamaterial-based MIMO antenna	Rogers 5880	24.8 × 40×0.25 mm^3)	3.30–4.45 GHz, 4.7–5.3 GHz, 7.7–8.25 GHz	unidirectional	Complex (MTM with SRR)	6.75	91
[20]	Planar antenna-based AMC	RT5880LZ	0.495×0.33×0.003/ (45 × 30 × 0.25 mm^3)	3.3–3.5 GHz	directional	Medium–Complex (DGS planar)	6	n/a
[22]	Modified L-shaped (4-element MIMO)	FR4	0.468×0.468 × 0.002/ (36×36×1.6 mm^3)	3.9–6.87 GHz	omnidirectional	Medium (planar)	2.53	77.26
[23]	FSS-based MIMO antenna with parasitic	Rogers 4350B	1.762× 1.423 × 0.45 (117.5×94.9×30 mm^3)	3–6 GHz	quasi-omnidirectional	Complex (FSS + parasitic)	7.96	97
[24]	two-element array with a matching network and DGS	FR4	0.305×0.305×0.002/ (30 ×30 ×1.6 mm^3)	3.05–6.32 GHz	omnidirectional	Complex (planar)	3.07	n/a
This work	Hybrid-geometry patch	FR4	0.27×0.34×0.01/ (46×58×1.6 mm^3)	1.77–9.55 GHz	omnidirectional	Low (planar single-layer)	3.39	72.8–95

Note: λ_L is the free-space wavelength at the lower operating frequency. Sim: Simulated. Structural complexity qualitatively reflects the requirement for additional electromagnetic structures, multilayer fabrication, external matching networks, parasitic superstrates, or advanced surface engineering techniques.

The antennas reported in [19, 20] demonstrate the application of electromagnetic surface-assisted and MTM-inspired techniques for improving radiation and impedance characteristics in Sub-6 GHz systems. The MTM-assisted MIMO antenna in [19] employs SRR-based loading to support gain enhancement and multiband behavior; however, the design involves a relatively sophisticated electromagnetic configuration together with directional radiation characteristics. Similarly, the AMC-integrated antenna presented in [20] improves radiation directivity through engineered surface structures, resulting in additional implementation complexity. The FSS-assisted antenna in [23] further achieves high gain and radiation efficiency using parasitic and superstrate elements, although the overall antenna profile becomes considerably larger. In addition, the antennas reported in [22, 24] demonstrate effective bandwidth-enhancement approaches for Sub-6 GHz applications. Nevertheless, the design in [22] operates over a comparatively narrower frequency range, whereas the array-assisted structure in [24] requires DGS and additional matching circuitry, leading to increased structural complexity.

By comparison, the proposed PHGWA realizes wideband performance through modal coupling between the hybrid radiator and the modified ground structure without requiring multilayer stacking, external matching networks, metamaterial loading, or superstrate integration. The proposed configuration maintains reliable impedance behavior and nearly omnidirectional radiation performance while retaining a straightforward fabrication process. Although the realized gain remains moderate at higher frequencies due to the limited effective aperture of the single-layer structure, the antenna offers a balanced trade-off among bandwidth, radiation stability, structural simplicity, and practical implementation for Sub-6 GHz 5G wireless applications.

IV. Conclusion

A planar hybrid-geometry wideband antenna for Sub-6 GHz 5G wireless applications has been proposed and experimentally characterized. The obtained broadband response mainly results from resonant-mode interaction between the hybrid radiating structure and the modified ground plane. Measured results confirm a −10 dB impedance bandwidth extending from 1.77 GHz to 9.55 GHz together with omnidirectional radiation behavior, practically realized gain, and acceptable radiation efficiency throughout the usable frequency range. The study further indicates that broadband operation can be achieved through geometry-driven current distribution and modal interaction without employing multilayer assemblies, parasitic superstrates, vias, external matching circuits, or metamaterial loading. Owing to its planar single-layer structure and relatively straightforward fabrication requirements, the proposed antenna may provide a suitable candidate for planar wideband wireless platforms operating in the Sub-6 GHz region. Future work will focus on extending the proposed configuration toward MIMO and pattern-reconfigurable systems for emerging wireless communication scenarios. Additional investigations concerning efficiency enhancement, fabrication tolerance, and environmental reliability will also be considered.

Conflict of Interest

The authors declare no conflict of interest.

Author Contributions

Suthasinee Lamultree conceived the study and methodology, collected and analyzed data, and wrote the paper. Chuwong Phongcharoenpanich is the supervisor of the research, and all authors have approved the final version.

Funding

This research project is supported by Rajamangala University of Technology Isan. Contract No. ENG8/69.

References

[1] Kapoor, R. Mishra, and P. Kumar, "Compact wideband printed antenna for sub-6 GHz fifth generation applications," *IJSSIS*, vol.13, no. 1, pp. 1–10, 2020.

[2] I. Ahmad, W. Tan, Q. Ali, and H. Sun, "Latest performance improvement strategies and techniques used in 5G antenna designing technology, a comprehensive study," *Micromachines*, vol. 13, no. 5, 717, 2022. doi: 10.3390/mi13050717

[3] H. Alwareth, I. M. Ibrahim, Z. Zakaria *et al.*, "A wideband high-gain microstrip array antenna integrated with frequency-selective surface for sub-6 GHz 5G applications, *Micromachines*, vol. 13, no. 8, 1215, 2022. doi: 10.3390/ mi13081215

[4] S. Al-Bawri, M.T. Islam, M.S. Islam *et al.*, "Massive metamaterial system-loaded MIMO antenna array for 5G base stations," *Sci. Rep.*, vol. 12, no. 1, 20 22. doi: 10.1038/s41598-022-18329-y

[5] S. K. Ibrahim, M. J. Singh, S. S. Al-Bawri *et al.*, "Design, challenges and developments for 5G massive MIMO antenna systems at Sub 6-GHz band: A review," *Nanomaterials*, vol. 13, no. 3, 520, 2023. doi: 10.3390/nano13030520

[6] M. K. Fattoum, S.M. Joujou, S.M. Ibrahim and H. El-Halabi, "Compact 5G broadband antenna for Sub-6 GHz wireless applications," *IEEE Access*, vol. 13, pp. 79444-79450, 2025. doi: 10.1109/ACCESS.2025.3566448

[7] M. Kaushal, S. Mukhopadhyay, and S. Roy, "Design of wideband planar antenna with inverted I-shaped tuning stubs for application in 5G, satellite communication, and Internet of Things," *Int. J. Commun. Syst.*, vol. 35, no. 11, e5191, 2022. doi: 10.1002/dac.5191

[8] H. A. El-Hakim, and H. A. Mohamed, "Engineering planar antenna using geometry arrangements for wireless communications and satellite applications," *Sci Rep*, vol. 13, 19196, 2023. doi: 10.1038/s41598-023-46400-9

[9] D. M. John *et al.*, "A wideband highly flexible CPW-fed antenna based on characteristic mode analysis for 5G wireless wearable sensor applications," *Results in Engineering*, vol. 23, 102412, 2024. doi: 10.1016/j.rineng.2024.102412

[10] A. Salisu, M. A. Elwanis, I. Elfergani *et al.*, "Machine learning-optimized compact wearable frequency reconfigurable antenna for sub-6 GHz/mm-wave 5G integration," *Sci Rep.*, vol. 15, 44912, 2025. doi:10.1038/s41598-025-28971-x

[11] Y. Rahayu, D. R. A. Pangestu, and C. H. Ku, "Compact triple-band monopole antenna with ACS-Fed for IoT devices on WLAN/WiMAX/5G/V2X networks," *IJEEETC*, vol. 14, no. 1, pp. 43–50, 2025. doi: 10.18178/ijeetc.14.1.43-50

[12] W. Balani, M. Sarvagya, A. Samasgikar *et al*., "Design and analysis of super wideband antenna for microwave applications," *Sensors*, vol. 21, no. 2, pp. 1–29, 2021. doi: 10.3390/s21020477

[13] A. Desai, M. Palandoken, J. Kulkarni *et al*., "Wideband flexible/transparent connected-ground MIMO antennas for Sub-6

GHz 5G and WLAN applications," *IEEE Access*, vol. 9, pp. 147003–147015, 2021. doi: 10.1109/ACCESS.2021.3123366
[14] L. Lazovi´c, B. Jokanovic, V. Rubežić *et al.*, "Fractal Cardioid slot antenna for super wideband applications," *Electronics*, vol. 11, 1043, 2022. doi:10.3390/electronics11071043
[15] N. Suguna and S. A. Revathi, "Compact super-wideband high bandwidth dimension ratio octagon-structured monopole antenna for future-generation wireless applications," *Appl. Sci*. vol. 13, 5057, 2023. doi: 10.3390/app13085057
[16] S. Salihovic and S. T. Imeci, "A stub microstrip patch antenna for sub 6GHz - 5G applications," *Heritage and Sustainable Development*, vol. 5, no. 1, pp. 99–106, 2023. doi: 10.37868/hsd.v5i1.104
[17] A. Bhattacharya, B. Roy, S. K. Chowdhury *et al*., "Design and analysis of a Koch snowflake fractal monopole antenna for wideband communication," *ACES*, vol. 32, no. 6, pp. 548–554, June 2017.
[18] P. Ramanujam, C. Arumugam, R. Venkatesan, and M. Ponnusamy, "Design of compact patch antenna with enhanced gain and bandwidth for 5G applications," *IET Microw. Antennas Propag.*, vol. 14, no. 12, pp. 1455–1461, 2020. doi: 10.1049/iet-map.2019.0891
[19] T. Saeidi, I. Ismail, S. Noghanian, A. R. H. Alhawari *et al*., "High gain triple-band metamaterial-based antipodal Vivaldi MIMO antenna for 5G communications," *Micromachines*, vol. 12, no. 3, 250, 2021. doi: 10.3390/mi12030250
[20] A. A. Abdulbari, S. K. A. Rahim, F. Abedi *et al*., "Single-layer planar monopole antenna-based artificial magnetic conductor (AMC)," *IJAP*, vol. 2022, 6724175, pp. 1–9, 2022. doi: 10.1155/2022/6724175
[21] M. Ayyappan and P. Patel, "On design of a triple elliptical super wideband antenna for 5G applications" *IEEE Access*, vol. 10, pp. 76031–76043, 2022. doi: 10.1109/ACCESS.2022.3185241
[22] R. Porwal, A. K. Rathor, M. V. D. Nair, and N. Raj, "A planar four-element modified L-shaped monopolar multiport antenna for sub-6 GHz applications," *AEU-Int. J. Electron. Commun.*, vol. 171, 154865, November 2023. doi: 10.1016/j.aeue.2023.154865
[23] M. Y. Zeain, M. Abu, A. A. Althuwayb *et al*., "A new technique of FSS-based novel chair-shaped compact MIMO antenna to enhance the gain for Sub-6GHz 5G applications," *IEEE Access*, vol. 12, pp. 49489–49507, 2024. doi: 10.1109/ACCESS.2024.3380013.
[24] M. M. Rahman, M. S. Islam, W. H. Yong *et al.*, "A wideband array antenna with a novel matching circuit and DGS structure for the sub 6 GHz applications," *Sci Rep.*, vol. 15, 14756, 2025. doi: 10.1038/s41598-025-99517-4
[25] B. Dwivedy, "Consideration of engineered ground planes for planar antennas: their effects and applications, a review," *IEEE Access*, vol. 10, pp. 84317–84329, 2022. doi: 10.1109/ACCESS.2022.3195507.
[26] A. Kumar and A. Kumar, "Defected ground structure based high gain, wideband and high diversity performance quad-element MIMO antenna array for 5G millimeter-wave communication," *PIER B*, vol. 101, pp. 1–16, 2023.
[27] A. Jamil, M. Rauf, A. Sami *et al*., "A Wideband hybrid fractal ring antenna for WLAN applications," *Int. J. Antennas Propag.*, 6136916, 2022.
[28] R. Parasher, D. Yadav, and A. Saharia, "Design and analysis of hybrid fractal frequency-band reconfigurable metamaterial antenna for multi-standard wireless applications," *Results in Engineering*, vol. 26, 104696, 2025. doi: 10.1016/j.rineng.2025
[29] S. Martin-Anton and D. Segovia-Vargas, "Fully planar dual-polarized broadband antenna for 3G, 4G and sub 6-GHz 5G base stations," *IEEE Access*, vol. 8, pp. 91940–91947, 2020. doi: 10.1109/ACCESS.2020.2994382
[30] T. Nahar, S. Rawat, P. Pathak *et al.*, "Leaf-shaped antennas for sub-6 GHz 5G applications," *IEEE Access*, vol. 12, pp. 114338–114357, 2024. doi: 10.1109/ACCESS.2024.3435528
[31] M. Khan and M. Chowdhury, "Analysis of modal excitation in wideband slot-loaded microstrip patch antenna using theory of characteristic modes," *IEEE Trans. Antennas Propag*., vol. 68, no. 11, pp. 7618–7623, Nov. 2020. doi: 10.1109/TAP.2020.2989867
[32] K. Zhang, P. J. Soh, T. Wu, M. Wang, and S. Yan, "A compact multimode antenna design based on metasurface for wideband applications," *IEEE Trans. Antennas Propag.*, vol. 72, no. 8, pp. 6747–6752, Aug. 2024. doi: 10.1109/TAP.2024.3408472
[33] M. A. Haque, R. A. Ananta, M. S. Ahammed *et al.*, "High-isolation dual-band MIMO antenna for next-generation 5G wireless networks at 28/38 GHz with machine learning-based gain prediction," *Sci Rep,* vol. 15, 20782, 2025. doi: 10.1038/s41598-025-02646-z.
[34] S. Lamultree, C. Jansri, and C. Phongcharoenpanich "Investigation of 3.1-10.6 GHz Circular Monopole Antenna with Modified Partial Ground Plane," *Przegląd Elektrotechniczny*, vol. 96, no. 4, pp. 49–52, 2020. doi: 10.15199/48.2020.04.09
[35] C. A. Balanis, *Antenna Theory: Analysis and Design*, 4th ed, Wiley, 2016.
[36] S. Lamultree, W. Thanamalapong, S. Dentri *et al.,* "Tri-band bidirectional antenna for 2.4/5 GHz WLAN and Ku-band applications," *Appl. Sci.*, vol. 12, no. 12, 5817. 2022, doi: 10.3390/app12125817

Suthasinee Lamultree received the B. Eng. and M. Eng. in telecommunication engineering from King Mongkut's Institute of Technology Ladkrabang, Thailand, in 2000 and 2003, respectively. In 2009, she received her D.Eng. in electrical engineering from the same institution. In 2016, she joined the Department of Electronics and Telecommunication Engineering, Faculty of Engineering, Rajamangala University of Technology Isan Khonkaen Campus, Khonkaen, Thailand. Her research interests include antenna design, microwave technology, and wireless communication systems.

Chuwong Phongcharoenpanich received his B.Eng. (Hons.), M.Eng., and D.Eng. degrees from King Mongkut's Institute of Technology Ladkrabang (KMITL), Bangkok, Thailand, in 1996, 1998, and 2001, respectively. Currently, he is a professor of telecommunications engineering at the Department of Telecommunications Engineering, KMITL. He also serves as the head of the Innovative Antenna and Electromagnetic Applications Research Laboratory. His research interests are antenna design for various mobile and wireless communication devices, conformal antennas, and array antenna theory.